Herre, Patrick; Will, Johannes; Dierner, Martin; Wang, Dong; Yokosawa, Tadahiro; Zech, Tobias; Wu, Mingjian; Przybilla, Thomas; Romeis, Stefan; Unruh, Tobias; Peukert, Wolfgang; Spiecker, Erdmann

Rapid fabrication and interface structure of highly faceted epitaxial Ni-Au solid solution nanoparticles on sapphire

Full Length Article

Rapid fabrication and interface structure of highly faceted epitaxial Ni-Au solid solution nanoparticles on sapphire

Patrick Herre [a],[1],[*], Johannes Will [b],[c],[**], Martin Dierner [b], Dong Wang [d], Tadahiro Yokosawa [b], Tobias Zech [c], Mingjian Wu [b], Thomas Przybilla [b], Stefan Romeis [a], Tobias Unruh [c], Wolfgang Peukert [a], Erdmann Spiecker [b],[**]

[a] *Institute of Particle Technology & Interdisciplinary Center for Functional Particle Systems, Friedrich-Alexander-Universität Erlangen-Nürnberg, Cauerstraße 4 & Haberstraße 9a, Erlangen 91058, Germany*
[b] *Institute of Micro- and Nanostructure Research & Center for Nanoanalysis and Electron Microscopy (CENEM), Friedrich-Alexander-Universität Erlangen-Nürnberg, IZNF, Cauerstraße 3, Erlangen 91058, Germany*
[c] *Crystallography and Structural Physics, Friedrich-Alexander-Universität Erlangen-Nürnberg, Staudtstraße 3, Erlangen 91058, Germany*
[d] *Materials for Electronics, Institute of Materials Science and Engineering & Institute of Micro- and Nanotechnologies, Technische Universität Ilmenau, Gustav-Kirchhoff-Straße 5, Ilmenau 98693, Germany*

ARTICLE INFO

ABSTRACT

Supersaturated Ni-Au solid solution particles were synthesized by rapid solid-state dewetting of bilayer thin films deposited onto *c*-plane sapphire single-crystals. Rapid thermal annealing above the miscibility gap of the Ni-Au system followed by quenching to room temperature resulted in textured and faceted submicron-sized particles as a function of alloying content in the range of 0–28 at% Au. Morphologically, the observed kinetic crystal shapes are confined by close-packed planes; in addition, high-index facets are identified as a function of alloying content by TEM cross-sectioning and equilibrium crystal shape simulations. All samples exhibit a distinct ⟨111⟩ out-of-plane as well as in-plane texture along densely packed directions. Lattice parameters extracted from independent orthogonal X-ray and electron diffraction techniques prove the formation of a solid solution without tetragonal distortion imposed by the sapphire substrate. At the particle-substrate interface of highly alloyed particles segregation of Au atoms as well as dislocations in stand-off position are found. These observations are in-line with a semi-coherent interface, where Au segregation is triggered by the reduction of the overall strain energy due to: (i) a lower shear modulus on the particle side of the interface, (ii) the shifting of misfit dislocations in stand-off position further away from the stiffer substrate and (iii) a reduction of intrinsic misfit dislocation strain energy on the tensile side. In addition, the mechanical properties of pure and alloyed particles were characterized by *in situ* compression experiments in the SEM. Typical force-displacement data of defect-free single-crystals were obtained, reaching the theoretical strength of Ni for particles smaller than 400 nm. Alloying changes the mechanical response from an intermittent and discrete plastic flow behavior into a homogeneous deformation regime at large compressive strain.

1. Introduction

Solid-state dewetting (SSD) of nanoscale thin metal films is a simple and efficient route for preparing supported particulate nanostructures on various substrates, including ceramic single-crystals like c-plane sapphire (α-Al$_2$O$_3$). Driven by the surface free-energy minimization, tailored particle morphologies with varying size and shape, density, composition, texture and intrinsic strain can be obtained as a function of annealing temperature, initial film thickness(es) and stacking sequence, atmosphere and substrate type [1–4]. Most notably, the recent gain in controllability of dewetting processes has established SSD as a large-scale and ro-

bust fabrication and patterning method for functional nanoarchitectures [5–9].

So far, mostly pure face-centered cubic (fcc) metal thin films deposited onto c-plane sapphire have been investigated (e.g. Al [10–12], Cu [13,14], Ni [15–17] and Au [18–20]) to elucidate mechanisms of SSD at early and advanced stages, equilibrium crystal shapes (ECS), or to gain fundamental insights into metal-ceramic interfaces. Typically, the partly dewetted films and resulting nanostructures exhibit both, a strong <111> texture parallel to the surface normal of the substrate and a pronounced in-plane orientation relationship along densely packed directions within the interface [10–17,20].

Alloying of (bilayer) thin films superimposes dewetting and texture evolution and provides additional energy contributions to the total energy balance. In particular, phase transformations and segregation effects may occur as a function of dewetting temperature in two-component films [21–24]. Besides fundamental studies, binary systems investigated so far are mostly related to the optimization of magnetic (CoPd [25], CoPt [26], FePd(Cu) [27, 28], NiAu [29], NiFe [30]), optical (AgAu [31–34], NiCu [35]) or catalytic (PtNi [36], NiCu [37], PtAu [38]) performances of the thus obtained particulate entities. As a general finding, alloying enhances the thermal stability, i.e., in comparison to the pure metal thin film the onset of SSD occurs at higher temperatures or longer annealing times [39–44]. However, the underlying mechanisms, the resulting ECS, including facet and texture evolution as a function of alloying content and thermal exposure are widely unknown.

The emphasis of this paper is to gain a better understanding of the morphological and structural evolution of alloyed particles formed at late stages of dewetting. However, we avoid long processing times by rapid thermal annealing (RTA) at high temperatures, a process commonly used in semiconductor industry. This process has already been successfully applied for the synthesis of catalytic PtNi particles on α-Al$_2$O$_3$ [36] and NiAu particles on SiO$_x$ [24,45–47]. In the present work, we focus on the influence of alloying for Ni-rich binary Ni-Au alloys due to several reasons:

1.1. Dewetting and interface structure

Besides missing fundamental studies of the interplay between dewetting, texturing and alloying of bilayer Ni-Au films on α-Al$_2$O$_3$, also interesting interface configurations as a function of Au content can be examined. For pure Ni particles dewetted on α-Al$_2$O$_3$, Meltzman et al. [16] describe the metal-ceramic interface that develops upon equilibration as "delocalized coherent", instead of semi-coherent or incoherent. Aberration-corrected TEM in conjunction with molecular statics simulations showed a periodic buckling of the terminating Ni layer adjacent to the interface. In this way, the interfacial misfit strain due to the large lattice mismatch of ~9% can be reduced by a local shift of atoms that reflect the coincidence symmetry of the two lattices. Upon alloying of Ni with Au, the lattice mismatch decreases up to a Au concentration of ~59 at% where matching for the Al$_2$O$_3$ d$_{30\bar{3}0}$ and NiAu d$_{220}$ lattice planes (at room temperature) between substrate and particle is obtained. As a result, a gradual change from a delocalized coherent interface to a semi-coherent interface composed of a misfit dislocation network and further to a coherent interface can be anticipated. However, also interface segregation of Au (as observed for Ni-Au on SiO$_2$ [48,49]) may convolute interface formation and structure. Hence, "A systematic experimental study of the influence of mismatch on interface reconstruction is a challenging task" [16].

1.2. Catalysis

The formation of faceted (Ni-Au) micro-/nanoparticles terminated by a high fraction of (111) and (100) planes and a high surface-to-volume ratio is of broad interest for heterogeneous catalysis [50–52]: for hydrogenation catalysis, Au has been found to improve selectivity over Ni-based catalysts [53–55], while hydrogenation activity is increased for Au by adding a group VIII metal [56,57]. The drawback of immiscibility in the Ni-Au system at low temperatures hinders progress in this field, although different wet chemical synthesis routes have recently shown potential applicability [50,58,59]. Rapid SSD of bilayer (Ni-Au) films by RTA processing for capping agent-free catalyst synthesis as alternative route has only sparsely been addressed yet [24,36,60].

1.3. Micromechanics

Particle formation via SSD of thin films is an irradiation-free approach to obtain small-scale samples without preparation-induced structural defects like, e.g., near-surface dislocations introduced by focused ion beam (FIB) preparation [61]. The thus obtained pristine particles are ideal specimens to unravel the truly active mechanisms of deformation of materials in confined dimensions. For example, Mordehai synthesized faceted and <111> textured submicron Au single-crystalline particles via SSD on α-Al$_2$O$_3$ [62]. The mechanical deformation behavior accessed by *in situ* scanning electron microscopy (SEM) compression experiments revealed a size-dependent onset of catastrophic yielding at stresses close to the theoretical shear strength of Au. The size effect was explained by finite element (FE) and molecular dynamics (MD) simulations to originate from the stress gradient along the active (111) {111}slip planes. Similar observations were made by different groups for Au [63,64], Ag [65] and Ni [66] particles. However, the influence of alloying on particle yielding and plasticity has not been addressed yet. Most interestingly, the Ni-rich side of the Ni-Au system may exhibit unique mechanical properties due to effects of solid solution strengthening resulting from the large mismatch of atomic radii (~15%).

Within the scope of this contribution, we first demonstrate the combination of solid-state dewetting and rapid thermal annealing to synthesize supersaturated and highly faceted Ni$_{1-x}$Au$_x$ nanoparticles over a wide concentration range of up to 28 at% Au. Second, the morphology, crystallographic texture (in- and out-of-plane), atomic interface structure, as well as elemental segregation at the interface and surface are investigated by a correlative approach utilizing advanced (transmission) electron microscopy and X-ray diffraction (XRD) techniques. Finally, the mechanical properties are characterized by *in situ* SEM compression testing. Overall, we present an elegant route to obtain particles with promising and tunable structural as well as mechanical properties by SSD at short processing times of only a few minutes.

2. Experimental

Pure Ni (99.995%) and bilayer Ni-Au (Au: 99.99%; both from ChemPUR, Germany) thin films were deposited by electron beam vapor deposition (HVB 130, Winter Vakuumtechnik, Germany) onto polished (0001)-oriented sapphire single-crystals (5 × 5 mm², 500 µm thickness, miscut angle < 0.3°, CrysTec Kristalltechnology, Germany). Different alloy compositions were adjusted by varying the thickness of the individual Ni and Au layers, while keeping the total film thickness (~40 nm) constant. Ni was always deposited as base layer to minimize oxidation during subsequent sample handling. More importantly, this particular stacking sequence having Au as top layer ensures fast intermixing of the constituents at elevated temperatures as investigated by Herz [67]. Table 1 summarizes the investigated samples.

Rapid thermal annealing was conducted in a Jetstar 100 furnace (Annealsys (formerly Jipelec), France, operated in a clean room fa-

Table 1
Thin film deposition and nominal alloy compositions.

Base layer thickness Ni/nm	Top layer thickness Au/nm	Binary alloy composition/ at% Au
40	0	0
37	3	5
34	6	10
30	10	18
25	15	28

cility) for 2 min at 970 °C in a reducing atmosphere (Ar:H$_2$ = 20:1) to induce solid-state dewetting above the miscibility gap of the Ni-Au system. The heating rate was set to 200 K/s, whereas fastest cooling was achieved by switching off the furnace (exponential temperature decay reaching 400 °C after 1 min [45,68]). This cooling rate is sufficient to avoid precipitation or spinodal decomposition [69].

Particle and particle-substrate interface characterization was carried out by correlative microscopy and scattering techniques. SEM (FE-SEM Gemini Ultra 55, Carl Zeiss, Germany) top and side view secondary electron (SE) imaging was performed at 2 kV and low beam current (< 10 pA, 10 μm objective aperture). To avoid charging effects, samples were sputter-coated (Baltec MED 020, Leica, Germany) with a ~5 nm thin amorphous carbon film. Site-specific focused ion beam (FIB) lamella preparation of individual particles was carried out in a Helios NanoLab 660 FIB microscope (Thermo Fisher, USA). Details on the protection layer deposition and Ga$^+$ ion milling parameters can be found elsewhere [70,71]. For conventional (C) and high resolution (HR) (S)TEM analysis of the FIB prepared samples a Titan³ Themis microscope (Thermo Fisher) was operated at 300 kV accelerating voltage. Images and selected area electron diffraction (SAED) patterns were acquired with a 4k CMOS camera. For chemical analysis by energy-dispersive X-ray spectroscopy (EDXS) the microscope is equipped with a Super-X^{TM} system composed of four silicon drift detectors.

XRD measurements in Bragg-Brentano geometry (out-of-plane) were carried out using an Empyrean diffractometer (PANalytical, the Netherlands). The X-ray source was equipped with Cu as anode material (λ = 0.15406 nm); a 2D solid-state detector (GaliPIX3D) operated in 1D scanning mode (7° (2θ) active length, 501 channels) was used for data acquisition. Samples were mounted on a flat sample stage and measured in an angular range of 20° - 100° (2θ). Step size and counting time were set to 0.007° (2θ) and 25 s/step, respectively. Pole figures and in-plane XRD scans were acquired using a SmartLab 9 kW diffractometer (Rigaku, Japan) with a rotating Cu anode setup, Johansson monochromator, parallel beam optics and in-plane soller slits with 0.5° angular acceptance. Surface sensitive in-plane scans under gracing incidence at 0.27° (θ_i) were performed in a small angular range (~10° (2χ)) around the (30$\bar{3}$0) α-Al$_2$O$_3$ reflection.

Micromechanical compression experiments were carried out with a custom-built manipulation device [72] operated in a conventional SEM (FE-SEM Gemini Ultra 55). Force-displacement data were acquired with resolutions of 10 μN and 5 nm, respectively; the probe displacement rate was 200 nm/s. A boron-doped diamond flat punch indenter with an initial plateau diameter of 2 μm was further thinned down to ~1 μm by FIB milling to adequately remove excessive particles before single particle compression. The procedure of the removal of particles next to the particle of interest is exemplarily illustrated within the supporting video file (V1). The electron beam was kept blanked during compression. SE images before and after (consecutive) compression were acquired with low dose imaging conditions.

3. Results

3.1. Particle morphology

Representative top view backscattered electron (BSE) and secondary electron (SE) images of rapidly dewetted and subsequently quenched pure Ni and binary Ni-Au samples are depicted in Fig. 1. On the left, low magnification BSE images give an overall impression of chemical homogeneity and particle morphology. As a general finding, the process of SSD progressed within the RTA processing time frame (~2 min) beyond the initial stages of void initiation and agglomeration to the stage of particle formation. Besides spherical particles (see white circles in case of pure Ni), elongated but faceted particle structures are discernible, which are far from their ECS according to Kaishew [73] and the Winterbottom construction [74]. In contrast, only spherical particles are observed for highly alloyed Ni-Au samples (18, 28 at%). Most interestingly, all spherical and non-spherical particles comprise a distinct flat top facet aligned parallel to the sapphire substrate. Samples of lower Au content (5, 10 at%), however, also contain irregularly shaped spheroidal particles exhibiting no clear facet relation with respect to the substrate (marked by red circles). Almost all particles show chemical homogeneity, few exceptions are encircled in green. Images for Ni-5 at% Au can be found within the Supplement (Fig. S1).

High magnification BSE and SE images of individual particles are shown in the middle column of Fig. 1, in combination with derived ECS simulations using the Zucker [75] software tool (right column). Typical low index facets can be observed for pure Ni: {111} colored in green, {100} in red and {110} in yellow. The top {111} facet is aligned parallel to the sapphire substrate. Besides closed-packed planes, also high-index facets like {210} in blue and {511} in cyan are found. The latter facet is unambiguously identified within the particle cross-section depicted in Fig. 3A and B, which was prepared and imaged along a [110] zone axis (ZA). For Ni-Au particles, the fundamental low-index facets are still present, however, their relative surface area has changed remarkably: in case of 10 & 18 at% Au, the {511} facets are dominant at the expense of {100} facet area. In addition, new high-index facets appear: {311} in violet and {331} in dark green. The highly alloyed 28 at% Au particles exhibit the same facets (except {311}) but with a more balanced facet area ratio. Similar to pure Ni, the Ni-28 at% Au particle cross-section prepared close to a [121] ZA (Fig. 3C and D) identifies most of the facets mentioned above.

3.2. Structure and orientation relation

Fig. 2 summarizes the out-of-plane and in-plane scattering data which were further complemented by pole figure measurements (see Fig. S2). XRD out-of-plane measurements in Bragg-Brentano geometry, which probe lattice planes aligned parallel to the substrate surface are displayed in Fig. 2A. Two main trends can be observed: (i) a systematic shift of the most intense 111 fcc Ni(-Au) reflection (and all other Ni(-Au) reflections) towards smaller scattering angles with increasing Au content and (ii) an increase of the 200 fcc Ni(-Au) reflection intensity for 5 at% Au (indicating a decrease of <111> out-of-plane texture), followed by a systematic decline up to the maximum Au content of 28 at%. Note the logarithmic intensity scale. Additional weak reflections are observed, originating from NiO$_x$ traces and a Au-rich alloy phase, which stems from Au segregation at surfaces and interfaces [44] (see Section 4.3). Moreover, a significant broadening of the Ni(-Au) reflections with increasing Au content is observed. The intrinsic peak width of the instrument is nicely captured by the 0006 Al$_2$O$_3$ reflection and is much smaller than the widths of the 111 fcc reflections. Neglecting thermal vibrations, an evolution of internal parti-
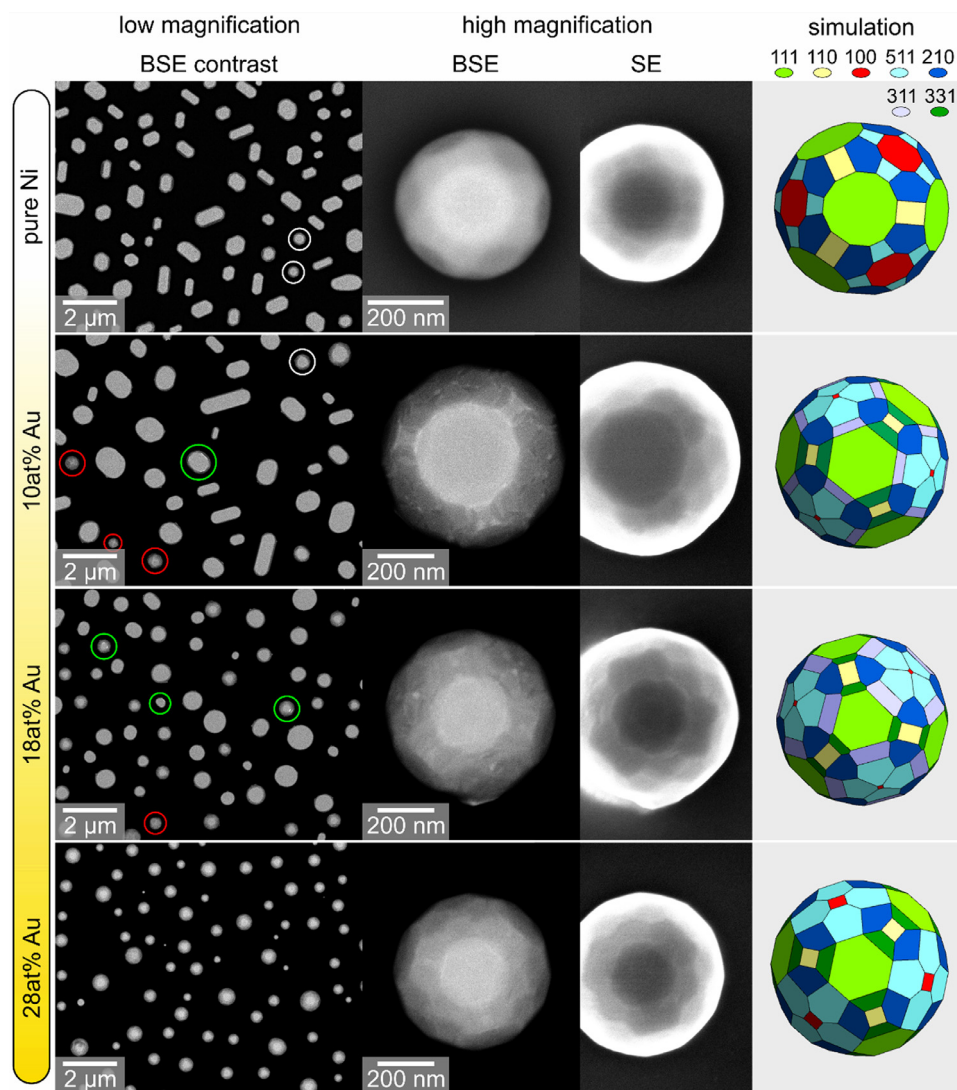
Fig. 1. Overview of RTA-processed (bilayer) thin films. The Au concentration increases from top to bottom. The topmost images correspond to pure Ni. Left column: low magnification BSE images; middle: BSE and SE of individual, equilibrated particles; right: ECS simulations using the Wulffmaker software [75]. For pure Ni and low Au concentrations (5, 10 at%), only few particles reach a spherical but faceted equilibrium shape (marked by white circles), while elongated particles/islands, which are far from their ECS, are prevalent. Particles highlighted by red and green circles indicate deviations from out-of-plane texture and chemical homogeneity, respectively. For the highest Au content, only spherical and highly faceted particles are discernible, having a distinct in-plane and out-of-plane texture. Corroborating ECS simulations reveal a multitude of low and high index facets, especially pronounced for alloyed particles.

cle strain and variations in particle composition are the remaining candidates for peak broadening.

To access the in-plane texture, pole figures of the 111 fcc Ni(-Au) reflection were recorded (see Fig. S2). For pure Ni, the observed sixfold symmetry of the 111 pole figure (i.e., symmetrically distributed {111} reflections) is caused by a twinned in-plane orientation relation and matches observations found in literature [16]. With increasing Au content, the sixfold symmetry evolves towards a threefold symmetry. Knowing the in-plane texture, we were able to conduct in-plane XRD measurements under grazing incidence conditions. The resulting scattering curves are displayed in Fig. 2B. Three main trends with increasing Au concentration are discernible: (i) a systematic shift of the $20\bar{2}$ fcc Ni(-Au) reflection towards smaller scattering angles, (ii) a broadening of the same reflection and (iii) an increase of the diffuse background around the $03\bar{3}0$ Al$_2$O$_3$ reflection. Qualitatively, the first observation is in-line with the out-of-plane measurements (Fig. 2A), both indicating an increase in cubic lattice parameters upon addition of Au. After extracting the lattice parameters this holds also quantitatively

(see Fig. 2C, overlapping red & blue data), revealing a fully relaxed cubic fcc Ni(-Au) lattice. No tetragonal distortion resulting from the epitaxial relationship to the substrate and/or thermal stresses upon cooling (due to considerably different thermal expansion coefficients of Ni(-Au) and Al$_2$O$_3$) could be detected. The 202 Ni(-Au) reflections are significantly broader compared to the internal Al$_2$O$_3$ reference reflection. Although the instrumental resolution for in-plane measurements is worse than for out-of-plane measurements, a quantitative evaluation is feasible since K$_{\alpha,2}$ contributions are avoided by using a Johansson monochromator to generate a solely K$_{\alpha,1}$ containing primary beam. Since we have not recognized strong variations in the chemical composition by SEM-EDX measurements, we attributed the peak width evolution to internal particle strain. After Gaussian subtraction of the intrinsic instrumental broadening width, the strain as function of Au content could be extracted for the specimens up to 18 at% Au. The evaluation (see Fig. S3) reveals an increase of internal strain with increasing Au content. Due to the proximity to the monotonically increasing diffuse background centered around the sapphire host
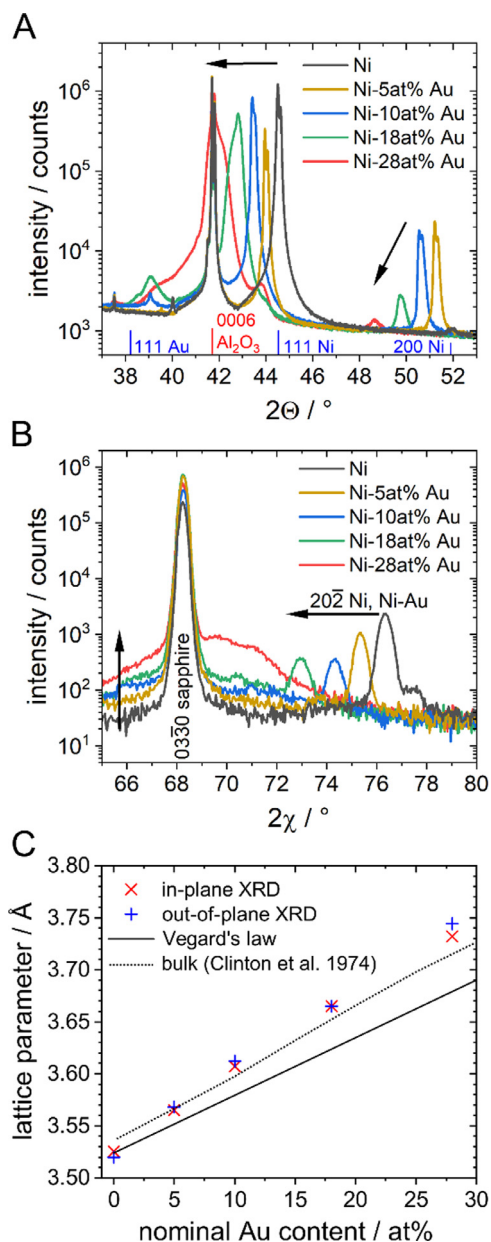
Fig. 2. (A) Out-of-plane X-ray data showing a strong ⟨111⟩ texture parallel to the substrate normal for pure Ni and highly alloyed particles, indicated by only minor contributions of the 200 Ni(-Au) reflection. Small alloying contents, however, decrease the out-of-plane texture (indicated by the inclined arrow). The continuous shift of the 111 reflection (horizontal arrow) proves the formation of a solid solution. (B) Correlative in-plane X-ray scans. Besides a shift of the 202 Ni(-Au) reflection, the diffuse background signal of the sapphire reflection increases as a function of alloying (vertical arrow). (C) Lattice parameters derived from A, (200 reflection) & B, (202 reflection).

reflection, the Ni(-Au) reflection width could not be evaluated for 28 at% Au.

The ensemble-averaged structural findings by different XRD techniques were corroborated by single-particle TEM evaluations of FIB prepared cross-sections of selected nicely faceted particles. In Fig. 3A and B, a bright-field (BF) TEM image and a corresponding selected area electron diffraction (SAED) pattern of the interface region are depicted for pure Ni. The sapphire substrate was aligned in a [10$\bar{1}$0] ZA using Kikuchi diffraction. By using a small SAED aperture, the interface region between particle and substrate was probed for determination of the crystallographic orientation relationship between particle and substrate: Besides the

sapphire reflections ([10$\bar{1}$0] ZA, red circles in B), also fcc Ni reflections characteristic for a [$\bar{1}$10] ZA are observed (encircled in blue). With the out-of-plane reflections of 111 fcc Ni and 0006 hcp sapphire being parallel, the orientation relation can be summarized as $(111)<\bar{1}10>_{Ni}$ || $(0001)<10\bar{1}0>_{Al2O3}$. Also, the particle surface facets can be identified by looking for *g* vectors that are perpendicular to a certain facet imaged edge-on in BF TEM; corresponding facet families are labeled in Fig. 3A. Following the Winterbottom equation, the solid-solid interface energy can be estimated using the surface energy of Ni $\gamma_{Ni(111)} = 2.14$ J/m² [15,76] and sapphire $\gamma_{Al2O3(0001)} = 1.25$ J/m² [77] at 970 °C. With the measured ratio $R_1/R_2 = 0.53$ (distances from Wulff point to interface and surface), the interface energy of Ni(111)//Al$_2$O$_3$(0001) equilibrated at 970 °C is computed to 2.38 J/m².

For Ni-28 at% Au, a similar analysis has been performed with a particle prepared in a [121] ZA (Fig. 3C,D). The SAED pattern taken at the interface reveals coincidence of the 111 fcc and 0006 hcp reflection; a peak splitting is observed for higher order reflections. Again, the in-plane orientation can be deduced from the identified ZA pattern for fcc Ni-Au ([$\bar{1}2\bar{1}$] ZA) and hcp sapphire ([$2\bar{1}\bar{1}0$] ZA). Hence, the orientation relation is $(111)<\bar{1}2\bar{1}>_{Ni}$ || $(0001)<2\bar{1}\bar{1}0>_{Al2O3}$. This orientation relation is identical to the one found for pure Ni, taking into account that the FIB cross sections in Fig. 3A–D reveal two different projections rotated by 30° around the substrate surface normal. Furthermore, the interface has been imaged by diffraction-contrast TEM using weak-beam dark-field (WBDF) and two-beam conditions. In Fig. 3E the WBDF image using a 202 reflection only a weak contrast at the interface is found. Similarly, the two-beam image (Fig. 3F) using the same reflection near a [221] ZA (∼30° sample tilt) only displays a Moiré contrast with a 4.76 nm periodicity, from which the lattice parameter for Ni-28 at% Au can be determined to 3.67 Å, compared to 3.74 Å as deduced from in-plane XRD.

3.3. Interface segregation

A minor segregation of Au to the interface and local surface sites can be observed within the STEM-HAADF image depicted in Fig. 4A (see white arrows). A higher magnification STEM-EDXS mapping of the right particle corner (B) in conjunction with the extracted concentration profile (C) along the orange arrow drawn in B proves an enrichment of Au in a ∼2 nm thick interface layer. The particle interior exhibits a homogeneous Ni/Au ratio of 73/27, close to the nominal composition.

3.4. Micromechanical compression behavior

Individual particle compression experiments were carried out for pure Ni (28 particles) and the highly alloyed Ni-28 at% Au sample (17 particles). The compressive deformation behavior is illustrated by consecutive compression steps in Fig. 5A, B. For data analysis, those experiments are omitted; furthermore, only particles close to their ECS are considered. During the actual compression, the pristine faceted half-spherical particles deform into a pancake-like flat cylinder. According to the side-view SE images the flow of material during plastic deformation is homogenously distributed. From top view, a flat but triangular-like shape evolves with characteristic linear surface steps. The Fast-Fourier-Transform (FFT) in Fig. 5A proves an orientation relation between surface steps of ∼60°. At large deformations, the conductive carbon surface layer delaminates from the material below. Morphologically, no differences between pure and alloyed particles are discernible.

In contrast, the recorded force-displacement data reveals significant differences, see Fig. 5C. After a linear loading segment, the force level drops suddenly (often denominated as pop-in or strain
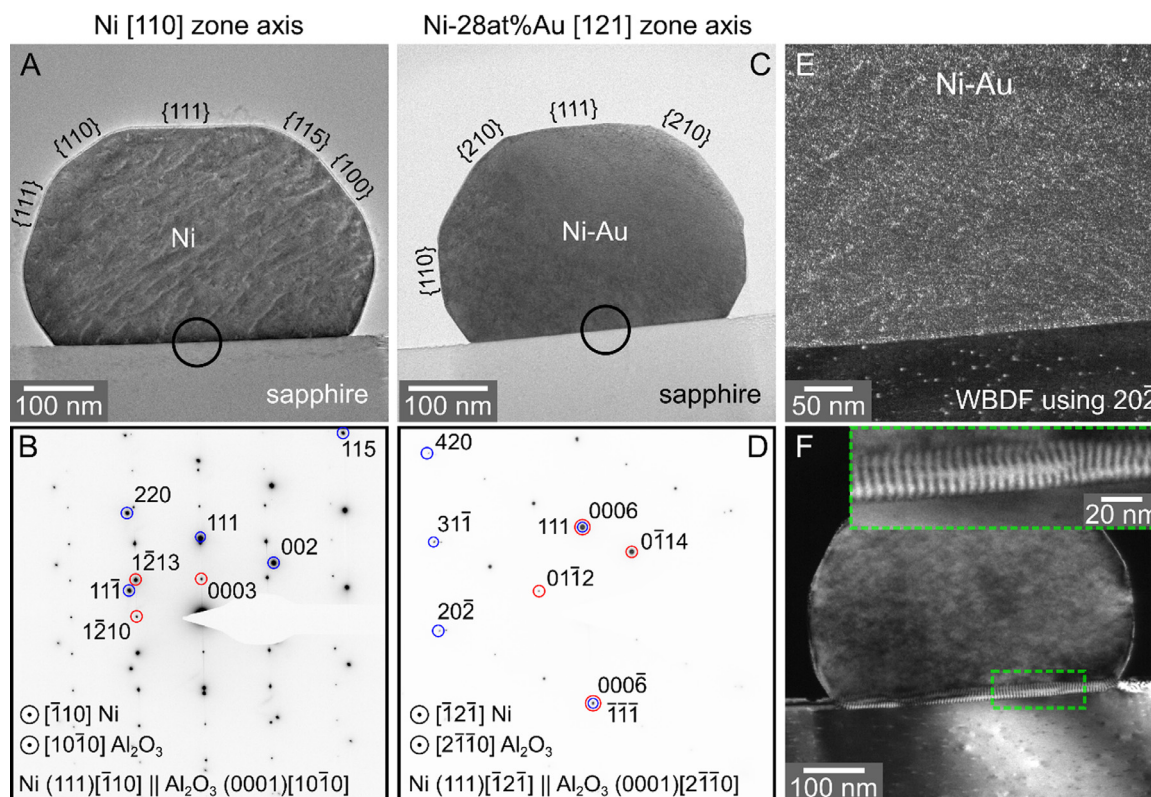
Fig. 3. Conventional TEM analysis of individual particles prepared by site-specific FIB milling. (A) BF TEM image of pure Ni along the $[\bar{1}10]$ imaging direction. (B) SAED pattern acquired at the interface region marked by the black circle in A, with Ni and sapphire reflections encircled in blue and red, respectively. (C) BF TEM of a highly alloyed 28 at% Au particle viewed along the $[\bar{1}2\bar{1}]$ ZA. (D) Corresponding SAED pattern of the interface region. The orientation relation between the Ni-Au particle and sapphire is identical to the relation found for pure Ni in B, only FIB prepared with an in-plane offset angle of 30° (E) Weak-beam dark-field image of C using the $20\bar{2}$ reflection. (F) Two-beam image at a sample tilt of ~30° near a [221] ZA. A Moiré contrast with a periodicity of 4.76 nm is visible at the interface.

burst [62]). This behavior is similar for both pure and alloyed particles. The subsequent elastic and plastic loading behavior is characterized by discrete flow events for pure Ni; the alloyed sample, however, displays homogeneous plastic flow. Data normalization (force/maximum initial particle cross section; displacement/initial height) yields one master curve for alloyed Ni-Au (red circles), whereas a strong scattering is observed for pure Ni (black and greyish data). Further analysis was confined to the evaluation of particle strength at the point of yielding. The axial compressive strength is estimated by dividing the maximum force at the elastic limit by the (original) surface area of the upper facet. Fig. 6 summarizes the obtained compressive strength data for pure and alloyed Ni(-Au) particles as a function of initial particle diameter.

Particles smaller than 400 nm reach the theoretical strength limit predicted by the model of Frenkel [78] for dislocation slip on {111} planes. The blueish data zone in Fig. 6 is confined by maximum shear stress values in the range of 15.4 GPa to 8.7 GPa for full dislocation {111} <110> slip and partial dislocation {111} <112> slip, respectively. Particles larger than 400 nm show a decrease in particle strength, irrespective of alloying content. The correlation of strength vs. sample size is often characterized by an inverse power law fit, however, the strong data scattering in Fig. 6 impedes a robust fitting.

4. Discussion

4.1. Particle morphology and ECS

The known ECS shape of Ni dewetted on sapphire is fully faceted, mainly composed of {111}, {100} and {110} surfaces as deduced from prolonged heating experiments [15,79]. In addition, high-index facets were observed as a function of oxygen partial pressure (p_{O2}): {531} and {831} facets at low p_{O2}, {210} and {310} facets at high p_{O2} [15]. In the present study, Ni particles processed at relatively low temperature and extremely short heating time are faceted with few rounded edges. Besides typical low-index facets, i.e. {111}, {100}, {110}, also {210} and {511} high-index facets were identified by imaging and simulations. Due to kinetic limitations, especially at lower temperature and simultaneously shorter processing time compared to former studies, the ECS is certainly not reached. Instead, the obtained particle morphology is henceforth denominated as *kinetic* or *growth shape*. This kinetic shape, which might also be influenced by stress [80] as present in the high misfit Ni-Au system, can serve as an indicator for specific facet families being stable at even lower temperatures [81,82]. The reason for the appearance of high-index facets is the increase of surface energy anisotropy for temperatures far below the melting point: Some fcc orientations exhibit energy minima or undergo a faceting-roughening transition (if surface diffusion is still sufficient). Those are facets of high planar density, e.g. {311}, {331}, {210} and {211} [82].

Alloying of Ni with Au significantly changes the kinetic shape towards a higher fraction of high-index facets of type {210}, {311}, {331} and {511}. Hence, the portion of low-index facets is lower compared to pure Ni. Similar observations were made by Nahor et al. [83] for Cr- and Cr-Fe-doped Ni particles equilibrated on yttrium stabilized zirconia (YSZ). The segregation of Cr to the particle surface is seen as a major factor causing a change in surface energy anisotropy and, hence, the growth shape or ECS. The influence of dopants by adsorption or segregation on crystal shapes has been observed for other systems as well [82,84,85]. From Fig. 4A and B, the segregation of Au to the particle surface and inter-
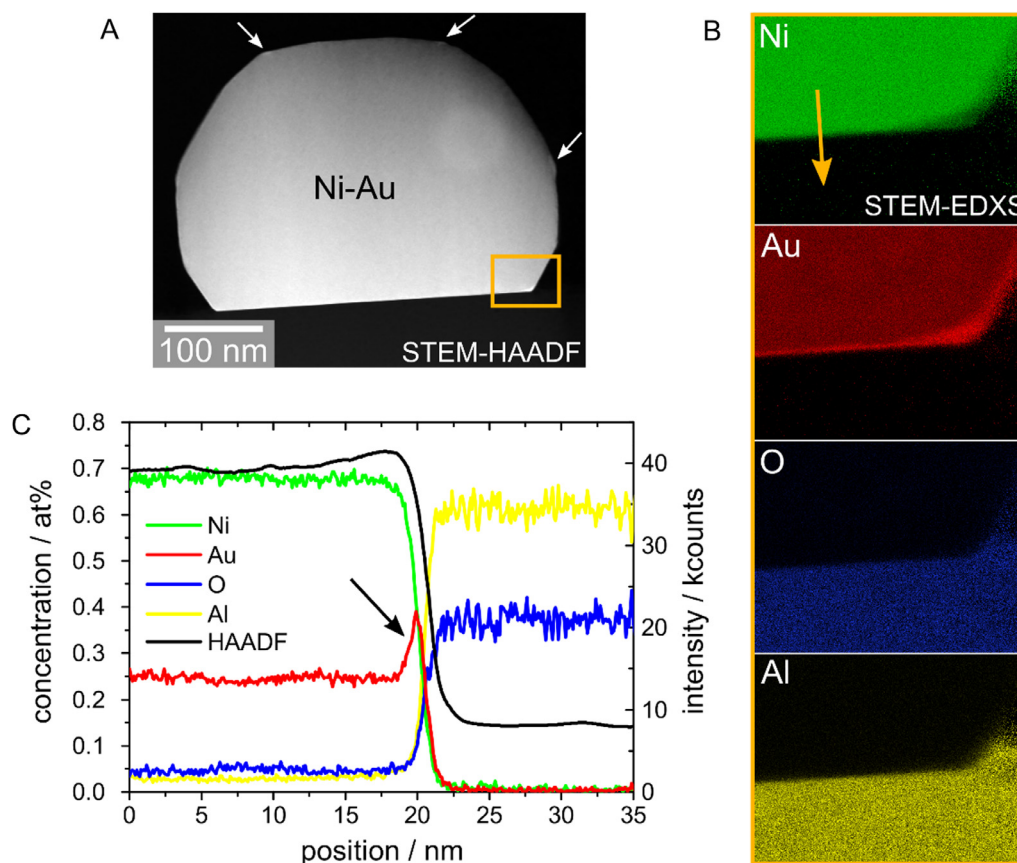
Fig. 4. (A) STEM-HAADF image of the particle depicted in Fig. 3C. White arrows mark minor Au segregation to the particle surface. (B) STEM-EDXS mappings (green: Ni, red: Au, blue: O, yellow: Al) of the orange framed particle corner in (A). A segregation of Au at the interface is evident, while chemical homogeneity is present within the particle. (C) Elemental concentration profile extracted along the orange arrow drawn in (B).

face is evident, yielding energetically changed surface energy ratios and maybe microscopic surface reconstruction. The influence of adsorbed species from the gas phase like oxygen or carbon during annealing can be neglected: All samples were heated within the same heating experiment in a pre-cleaned furnace under reducing atmosphere.

In addition, alloying with Au reduces the fraction of elongated and non-spherical particles, which demonstrates that the diffusion mechanism as rate limiting step is altered with increasing Au content. Indeed, higher self- and interdiffusion coefficients for Au and Ni are reported with increasing Au content for Ni/Au bulk alloys [86].

4.2. Particle structure and texture

A comparison of the lattice parameter as a function of Au content with Vegard's law [87] and experimental data from bulk samples [88] is plotted in Fig. 2C. The expected deviation from Eymery et al.'s law [89,90] follows that of Ni-Au bulk alloys. The difference can be attributed to uncertainties in chemical composition (see Table 1 in SI) and should not be attributed to a size effect.

Although alloying does not change the predominant ⟨111⟩ texturing nor the in-plane alignment along densely packed directions as reported for pure and doped Ni particles before [16,83], it influences the ratio of the observed twin variants, where one twin variant grows on expense of the other. A similar observation was recently made for the Ni-Fe system [30], where differences in the 2nd & 3rd layer configuration were identified as driving force.

Interestingly, the evolution of texture is almost fully completed within the processing time of 2 min. The temporal interplay between texture formation and dewetting was studied for thin Au films on amorphous SiN_x membranes by *in situ* heating experiments in the TEM [91]: Texture evolution is found to be highly correlated with the process of dewetting, as material agglomerates into preferentially oriented grains. The same holds true for the Ni-Au bilayer configuration investigated in this study, whereby the crystalline substrate and resulting epitaxial orientation relationship plays an additional role. Time- and temperature-resolved diffraction experiments may shed further light on the interplay between texture evolution and intermixing of bilayer Ni-Au in the first stage of SSD.

4.3. Au segregation and interface structure

Segregation of Au is observed towards the free surface of the particle as well as to the particle-substrate interface (see Fig. 4). The amount of Au excess in atoms per nm² can be estimated by calculating the planar density of the aligned {111} fcc lattice planes, which is 16.5 atoms/nm² ($PD_{111} = 4/\sqrt{3}a^2$). For this quantification, the lattice spacing of ∼3.74 Å from the XRD measurements was utilized. A typical excess of ∼10–20 at% was observed yielding an Au excess at the interface of ∼1.65-3.30 atoms/nm².

The segregation of Au towards the particle surface at temperatures above the miscibility gap of the Ni-Au system is driven by the energy contribution of the surface. Considering the {111} surface energies of Au (1.40 J/m² [18]) and Ni (2.14 J/m²) at 970°C, Au atoms are energetically favored to occupy surface sites. Moreover, the large atomic size misfit or strain between Ni and Au leads to a further driving force for segregation as demonstrated by Kelley et al. for Ni-rich (1 at% Au) and Au-rich (1 at% Ni) alloys at 700°C
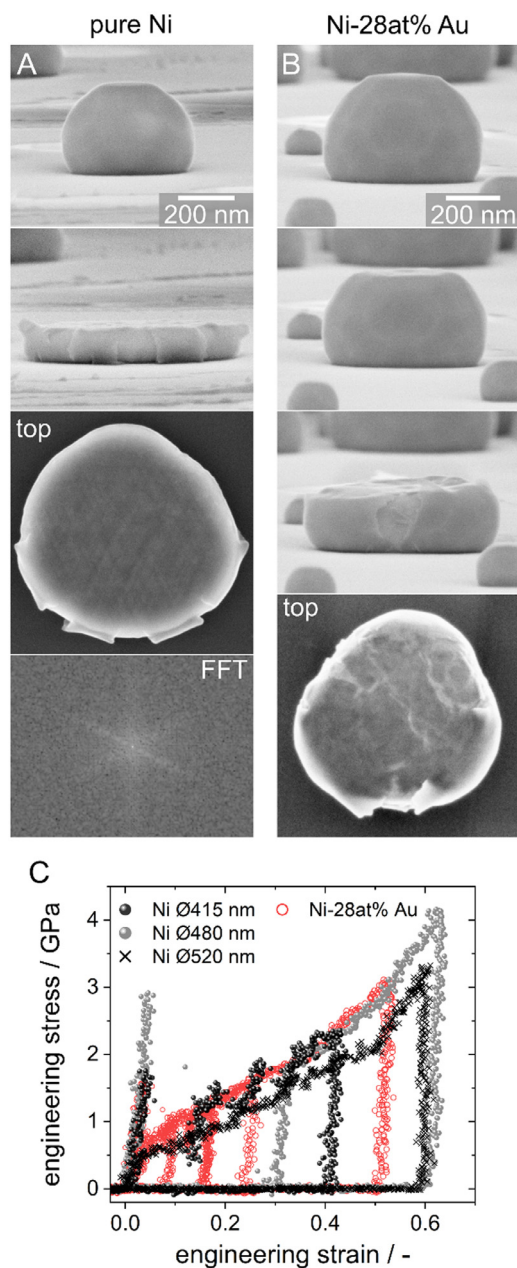
pure Ni

Ni-28at% Au

Fig. 5. Micro-compression testing in the SEM. Consecutive SE side view images during the compression of pure Ni (A) and alloyed Ni-Au (B) particles illustrate homogeneous deformation. Corresponding top view images are obtained after remounting the sample wafer. The FFT of the inner particle region in top view proves dislocation motion along {111} <110>. (C) Force-deformation data of alloyed particles converge to one master curve after normalization (red circles). Data for pure Ni (black and gray circles) exhibit strong scattering and discrete flow events.

Fig. 6. Axial compressive strength and critical resolved shear stress (CRSS) for {111}<110> dislocation slip. Greyish (Ni) and reddish (Ni-Au) data overlap in the same particle size range. Particles < 400 nm reach the theoretical strength limit of pure Ni (blueish zone).

[92]. Experimental data and pair-potential modeling suggest an enrichment of Au at the surface for both alloy compositions.

As can be inferred from the high magnification BSE images in Fig. 1 for 10 and 18 at% Au as well as the HAADF STEM image in Fig. 4A, surface segregation is not homogeneous. Local surface sites enriched with Au are confined to regions near the 100 and 210 surface facets, respectively. These findings corroborate experimental results by the group of Wynblatt, which show surface segregation anisotropy of Au detected by Auger microprobe analysis in a Ni-0.1 at% Au alloy up to 900°C [93,94]. The highest Au concentrations were found close to 100 and 210 poles.
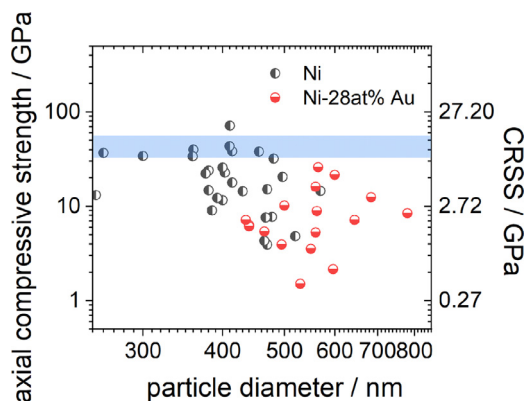
In contrast, the segregation of Au to the particle-substrate interface as depicted in Fig. 4C cannot be understood from an interface energy consideration: Although not measured at identical conditions, the almost similar interface energies of Ni//sapphire (2.16 J/m² [16]) from samples equilibrated at a very low oxygen partial pressure like in our work and Au//sapphire (2.15 J/m² [18]) from samples annealed in air do not explain this segregation phenomena. Note that in this context a very low oxygen partial pressure might change the termination and lead to metal-metal bonds at the interface [95], thus changing the interface energy.

In contrast, even a Ni segregation is expected for a metal/oxide interface since Ni exhibits the higher oxide forming tendency as compared to Au [96]. All these arguments point towards a reduction of the total strain energy of the system as driving force for Au segregation. To shed further light on this hypothesis, another 28 at% Au particle cross-section was prepared in a [110] ZA with a final thickness of ∼30 nm.

Fig. 7A validates the ∼2 nm thin Au segregation layer at the interface (cf. Fig. 4). Note the Au/Ni ratio beyond ∼13 nm is not meaningful, since it is extracted from background EDX noise acquired within the Al_2O_3 substrate. A detailed high resolution STEM analysis using ADF and HAADF signals is depicted in Fig. 7B and C. The ADF signal reveals a bright contrast line directly at the interface. Such bright interface contrast in ADF images has been attributed to lattice strain [97], in particular at larger sample thickness as in the present case [98]. The width of the bright contrast line amounts to ∼0.45 nm, which is in the range of one interfacial d_{111} Ni(-Au 28 at%) layer and one d_{0006} layer of sapphire. Within the HAADF image, a misfit dislocation is found in a stand-off position [99], namely one atomic layer away from the interface.

By combining this information, the confined ADF signal can be at least partly attributed to local strain associated with misfit dislocations [100], which are expected to form a dense two-dimensional (hexagonal or triangular) network at the interface [101]. For the present lattice mismatch of ∼4.0% as calculated from the d_{202} spacing of Ni(-Au 28 at%) and d_{0330} spacing of sapphire, the spacing of misfit dislocations in this network is expected to be in the range of a several nanometers depending on whether a/2<110> perfect or a/6<112> partial dislocation are present. Considering the fact that the TEM lamella is ∼30 nm thick, projection effects are expected to complicate the interpretation of lattice fringe contrast and it is even astonishing that a quite clear edge-on dislocation contrast is revealed. Even though a relaxation of the dislocation structure in the thin TEM lamella cannot be excluded we try to determine the Burgers vector (BV) of the dislocation in stand-off position by performing a Burgers circuit in the HAADF-STEM im-
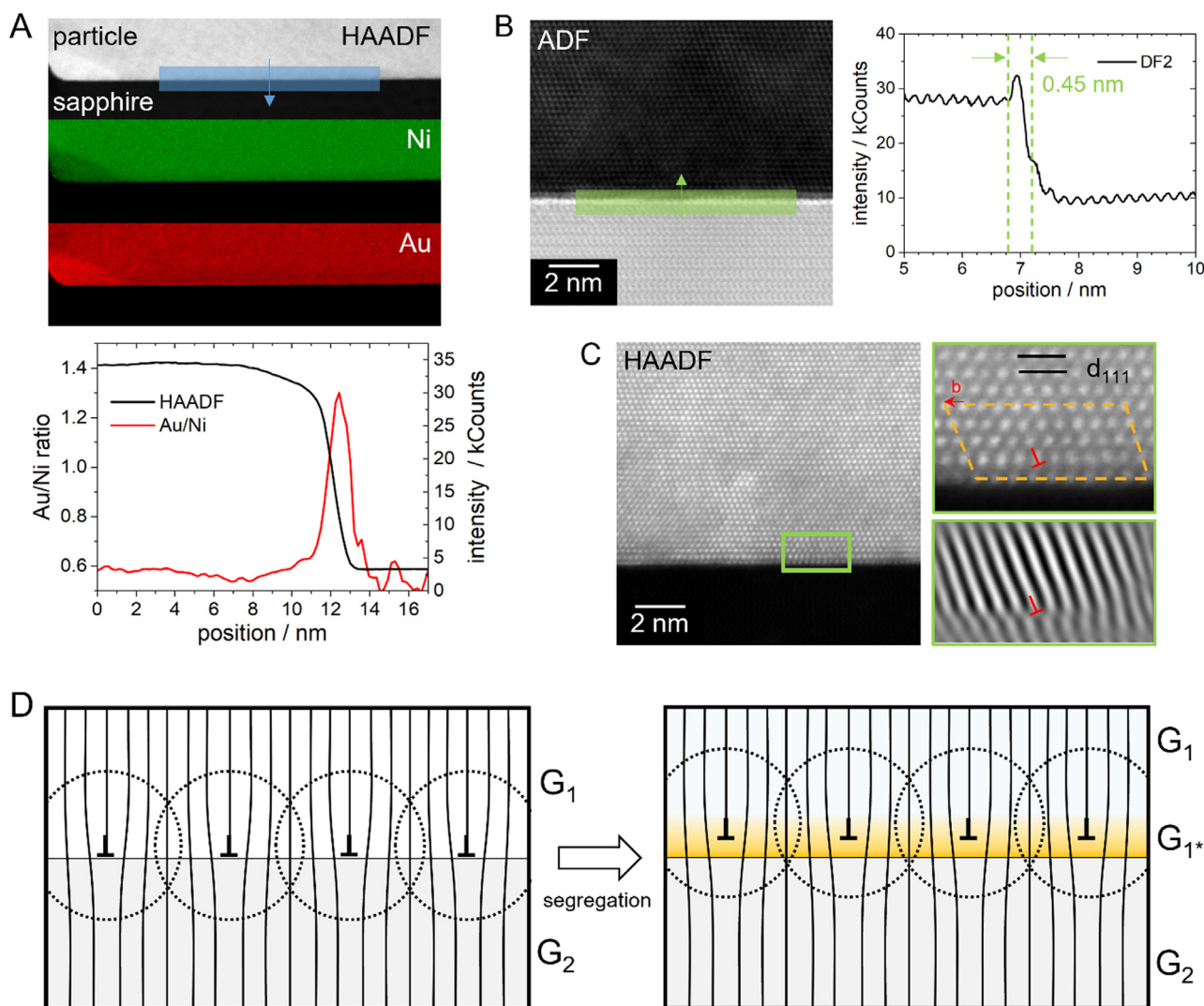
Fig. 7. STEM-EDXS mapping of a 28 at% Au particle prepared in [110] ZA clearly revealing Au segregation at the interface (A). The drop in the Au/Ni ratio profile towards the substrate cannot be interpreted since both elements are absent in the substrate. HRSTEM ADF (B) and HAADF (C) images of the interface reveal a confined ~ 0.45 nm thin strained region and the presence of misfit dislocations, respectively. The Burgers circuit analysis shows a projected BV of type a/4<112>, corresponding to the projection of a perfect a/2<110> dislocation into the image plane. In (D) the role of Au segregation on the (out-of-plane) position of misfit dislocations and the overall reduction of the shear modulus ($G_{1*} < G_1 << G_2$) at the interface to reduce the total strain energy is depicted.

age (Fig. 7C). However, due to the close proximity of the interface a precise determination of the BV is not possible as there is only one atomic layer between the dislocation core and the interface. According to the Burgers circuit depicted in Fig. 7C the closure error appears to be of type a/4<112> (see arrow), which would correspond to the projection of an inclined a/2<110> BV (of a 30° perfect dislocation) into the image plane. However, within the precision of the analysis the BV could be equally of type a/6<112>, corresponding to a 90° partial dislocation, which is more likely as pure edge dislocations most efficiently relax lattice misfit [101–103].

The importance of strain fields originating from lattice mismatch and misfit dislocations at the interface extending towards both the substrate and the particles becomes obvious in the surface sensitive in-plane X-ray diffraction data (Fig. 2B). Here, a monotonic increase of the diffuse background around the sapphire reflection with increasing Au concentration is found, which typically originates from strain fields in the otherwise perfect crystal lattice [104–106]. In this context, an increasing particle lattice constant with increasing Au concentration leads to a lower misfit and thus misfit dislocation density, which in turn results in strain field

contributions reaching further into both the substrate and the particles. Indeed, as stated in [103] the spatial extension of the dislocation strain fields perpendicular to the interface is of the same order as the in-plane spacing of dislocations in the interface. This supports the interpretation that less confined strain fields are the origin of the observed increase of the diffuse background.

Beyond this purely structural consideration, we identified a clear segregation of Au to the interface (Fig. 7A) and propose that this segregation is driven by a reduction of total strain energy in both the particle and the substrate. First, due to a higher shear modulus of Ni ($G = 76$ GPa) compared to Au ($G = 27$ GPa), the shear modulus of the NiAu solid solution is considerably decreased by local segregation of Au. This directly decreases the strain energy of the dislocation network and is expected to further increase the stand-off position, as the particle lattice becomes even less stiff compared to the sapphire substrate [99]. As a result, the dislocation strain fields penetrate less deeply into the much stiffer sapphire substrate which further reduces the total strain energy. Moreover, besides a reduction in shear modulus, segregation of the considerably larger Au atoms (compared to Ni) to the tensile side of the misfit dislocations further reduces the total strain energy. A

sketch illustrating the aforementioned contributions and the role of G for reduction of the total energy of the semi-coherent interface is depicted in Fig. 7D.

4.4. Deformation behavior

The compressive strength of pure Ni nano-/microparticles dewetted on sapphire has been studied recently by Sharma [66]. Although these particles were prepared at higher temperature (1050°C) and longer annealing time (12 h), similar strength values are obtained for pure Ni particles in the present study approaching the theoretical strength of Ni for particles smaller than 400 nm (see Fig. 6). The nucleation of full dislocations in the otherwise pristine and dislocation-free crystal as carrier of plasticity was identified by MD simulations [66], which is also the case for our Ni particles as inferred from the surface step arrangement after compression (see Fig. 5A). The compressive strength of alloyed particles follows the same trend as pure Ni, however, slightly larger particles due to Au facilitated growth of the initial grains [43] have been tested. Therefore, no concluding remark can be given related to the size-dependency of strength in alloyed particles or a slightly lower theoretical strength value. Considering the theoretical strength as a portion of the shear modulus, a lower theoretical strength is expected for Ni-Au alloys.

Most interestingly, the plastic deformation for compressive strains beyond the yield point shows significant differences. Intermittent, discrete flow events as in pure Ni are not observed for alloyed particles, only a continuous plastic flow without significant hardening. While the former has been frequently observed in pure small- and large-scale specimens [107,108], the latter phenomena can be attributed to the interaction of nucleated dislocations with solute Au atoms. Here, micro-compression tests at various strain-rates could be employed in the future to determine characteristic dislocation activation volumes and energies in order to decipher the truly active deformation process [109].

5. Summary and conclusion

In this work, we present an elegant route to fabricate supported supersaturated Ni-Au nanoparticles with tunable composition and properties in short processing times at a cm² scale by combining solid-state dewetting and rapid thermal annealing. By correlating results from advanced electron microscopy, X-ray diffraction and micromechanical testing, a comprehensive insight into the structure and properties is presented:

- Particle formation and texture evolution are completed within 2 min processing time. Highly textured, faceted and capping agent-free particles suitable for catalysis can be fabricated. The ratio of high and low-index facets can be tuned by changing the initial ratio of the Au/Ni bilayer films.
- Out-of-plane and in-plane X-ray diffraction, electron diffraction as well as STEM-EDX consistently reveal that the NiAu particles are successfully quenched-in as homogeneous solid solution with fully relaxed cubic lattice, i.e. thermal stresses resulting from the considerably different thermal expansion coefficients of NiAu and the sapphire substrate are fully released.
- The interplay of solute atoms and the substrate manifests in a minor segregation of Au at the surface and interface, the growth of one twin variant on expense of the other and strain within the substrate as revealed by an increase in the diffuse X-ray scattering background. The semi-coherent nature of the interface including the reduction of the total strain energy acts as driving force for the nanoscale interface segregation of Au within Ni-rich particles.

- Tuning the particle size by reducing the overall bilayer thickness, amplifying Au segregation to specific facets by intentionally heating below the solubility gap or combining the particles with light harvesting oxides like TiO_2 or ZnO can be explored in future to optimize particles for catalytic applications.
- Particles below 400 nm are intrinsically free of extended defects, thus approaching the theoretical strength of Ni.
- The interaction of solute Au atoms with nucleated dislocations leads to a fundamental change from an intermittent and discrete plastic flow behavior into a homogeneous deformation regime at large compressive strain.

Declaration of Competing Interest

The authors declare that they have no known competing financial interests or personal relationships that could have appeared to influence the work reported in this paper.

Supplementary materials

Supplementary material associated with this article can be found, in the online version, at doi:10.1016/j.actamat.2021.117318.

References

[1] C.V. Thompson, Solid-state dewetting of thin films, Annu. Rev. Mater. Res. 42 (1) (2012) 399–434.

[2] D. Wang, P. Schaaf, Solid-state dewetting for fabrication of metallic nanoparticles and influences of nanostructured substrates and dealloying, Phys. Status Solidi A 210 (8) (2013) 1544–1551.

[3] F. Leroy, et al., How to control solid state dewetting: a short review, Surf. Sci. Rep. 71 (2) (2016) 391–409.

[4] R.A. Hughes, E. Menumerov, S. Neretina, When lithography meets self-assembly: a review of recent advances in the directed assembly of complex metal nanostructures on planar and textured surfaces, Nanotechnology 28 (28) (2017) 282002.

[5] P. Farzinpour, et al., Dynamic templating: a large area processing route for the assembly of periodic arrays of sub-micrometer and nanoscale structures, Nanoscale 5 (5) (2013).

[6] F. Ruffino, M.G. Grimaldi, Controlled dewetting as fabrication and patterning strategy for metal nanostructures, Phys. Status Solidi A 212 (8) (2015) 1662–1684.

[7] M. Naffouti, et al., Complex dewetting scenarios of ultrathin silicon films for large-scale nanoarchitectures, Sci. Adv. 3 (11) (2017).

[8] J. Ye, D. Zuev, S. Makarov, Dewetting mechanisms and their exploitation for the large-scale fabrication of advanced nanophotonic systems, Int. Mater. Rev. 64 (8) (2018) 439–477.

[9] C. Clarke, et al., Large-scale dewetting assembly of gold nanoparticles for plasmonic enhanced upconversion nanoparticles, Nanoscale 10 (14) (2018) 6270–6276.

[10] D.L. Medlin, et al., Orientation relationships in heteroepitaxial aluminum films on sapphire, Thin Solid Films 299 (1–2) (1997) 110–114.

[11] G. Dehm, B.J. Inkson, T. Wagner, Growth and microstructural stability of epitaxial Al films on (0001) α-Al_2O_3 substrates, Acta Mater. 50 (20) (2002) 5021–5032.

[12] S.W. Hieke, et al., Microstructural evolution and solid state dewetting of epitaxial Al thin films on sapphire (α-Al_2O_3), Acta Mater. 133 (2017) 356–366.

[13] G. Dehm, et al., Synthesis of analytical and high-resolution transmission electron microscopy to determine the interface structure of Cu/Al_2O_3, Ultramicroscopy 67 (1–4) (1997) 207–217.

[14] S. Curiotto, et al., Orientation relationships of copper crystals on c-plane sapphire, Acta Mater. 59 (13) (2011) 5320–5331.

[15] H. Meltzman, et al., The equilibrium crystal shape of nickel, Acta Mater. 59 (9) (2011) 3473–3483.

[16] H. Meltzman, D. Mordehai, W.D. Kaplan, Solid-solid interface reconstruction at equilibrated Ni–Al_2O_3 interfaces, Acta Mater. 60 (11) (2012) 4359–4369.

[17] E. Rabkin, D. Amram, E. Alster, Solid state dewetting and stress relaxation in a thin single crystalline Ni film on sapphire, Acta Mater. 74 (2014) 30–38.

[18] H. Sadan, W.D. Kaplan, Au-sapphire (0001) solid–solid interfacial energy, J. Mater. Sci. 41 (16) (2006) 5099–5107.

[19] A. Kosinova, et al., Mechanisms of solid-state dewetting of thin Au films in different annealing atmospheres, Acta Mater. 83 (2015) 91–101.

[20] A. Serrano, et al., Nanostructured Au(111)/oxide epitaxial heterostructures with tailoring plasmonic response by a one-step strategy, J. Phys. Chem. C 123 (41) (2019) 25294–25302.

[21] H. Chen, J. Zuo, Structure and phase separation of Ag–Cu alloy thin films, Acta Mater. 55 (5) (2007) 1617–1628.

[22] D. Wang, P. Schaaf, Ni-Au bi-metallic nanoparticles formed *via* dewetting, Mater. Lett. 70 (2012) 30–33.

[23] D. Amram, L. Klinger, E. Rabkin, Phase transformations in Au(Fe) nano- and microparticles obtained by solid state dewetting of thin Au–Fe bilayer films, Acta Mater. 61 (14) (2013) 5130–5143.

[24] A. Herz, et al., Facet-controlled phase separation in supersaturated Au-Ni nanoparticles upon shape equilibration, Appl. Phys. Lett. 107 (7) (2015).

[25] R. Esterina, et al., Solid-state dewetting of magnetic binary multilayer thin films, J. Appl. Phys. 118 (14) (2015).

[26] Y.J. Oh, et al., Templated assembly of Co-Pt nanoparticles *via* thermal and laser-induced dewetting of bilayer metal films, Nanoscale 5 (1) (2013) 401–407.

[27] T. Schied, et al., Fe-Pd thin films as a model system for self-organized exchange coupled nanomagnets, J. Appl. Phys. 108 (3) (2010).

[28] M. Krupinski, et al., Ordered FePdCu nanoisland arrays made by templated solid-state dewetting, Nanotechnology 26 (42) (2015).

[29] L. Wang, et al., Magnetic-plasmonic Ni@Au core-shell nanoparticle arrays and their SERS properties, RSC Adv. 10 (5) (2020) 2661–2669.

[30] A. Sharma, et al., Grain growth and solid-state dewetting of Bi-crystal Ni-Fe thin films on sapphire, Acta Mater. 168 (2019) 237–249.

[31] A. Goswami, S. Aravindan, P.V. Rao, Fabrication of substrate supported bimetallic nanoparticles and their optical characterization through reflection spectra, Superlattices Microstruct. 91 (2016) 252–258.

[32] M. Kang, et al., Bioplasmonic alloyed nanoislands using dewetting of bilayer thin films, ACS Appl. Mater. Interfaces 9 (42) (2017) 37154–37159.

[33] D. Wang, P. Schaaf, Plasmonic nanosponges, Adv. Phys. X 3 (1) (2018).

[34] D. Wang, P. Schaaf, Synthesis and characterization of size controlled bimetallic nanosponges, Phys. Sci. Rev. 4 (6) (2019).

[35] Y. Wu, J.D. Fowlkes, P.D. Rack, The optical properties of Cu-Ni nanoparticles produced *via* pulsed laser dewetting of ultrathin films: the effect of nanoparticle size and composition on the plasmon response, J. Mater. Res. 26 (2) (2011) 277–287.

[36] O. Seo, et al., Controlling the alloy composition of PtNi nanocrystals using solid-state dewetting of bilayer films, J. Alloys Compd. 667 (2016) 141–145.

[37] D. Spanu, et al., Templated dewetting-alloying of NiCu bilayers on TiO2 nanotubes enables efficient noble-metal-free photocatalytic H2 evolution, ACS Catal. 8 (6) (2018) 5298–5305.

[38] H.W. Lee, Solid-solution alloying of immiscible Pt and Au boosts catalytic performance for H2O2 direct synthesis, Acta Mater. (2021) 205.

[39] H.C. Kim, N.D. Theodore, T.L. Alford, Comparison of texture evolution in Ag and Ag(Al) alloy thin films on amorphous SiO2, J. Appl. Phys. 95 (9) (2004) 5180–5188.

[40] Y. Minamide, et al., Agglomeration suppression behavior and mechanisms of Ag-Cu and Ag-Nb thin films, Vacuum 84 (5) (2009) 657–662.

[41] B.-J. Park, et al., Improving the thermal stability of nickel monosilicide thin films by combining annealing with the use of an interlayer and a capping layer, J. Vac. Sci. Technol. A Vac. Surf. Films 29 (3) (2011).

[42] D. Amram, L. Klinger, E. Rabkin, Anisotropic hole growth during solid-state dewetting of single-crystal Au-Fe thin films, Acta Mater. 60 (6–7) (2012) 3047–3056.

[43] C. Manuela Müller, R. Spolenak, Dewetting of Au and AuPt alloy films: a dewetting zone model, J. Appl. Phys. 113 (9) (2013).

[44] H. Barda, E. Rabkin, Improving the thermal stability of nickel thin films on sapphire by a minor alloying addition of gold, Appl. Surf. Sci. 484 (2019) 1070–1079.

[45] A. Herz, et al., Formation of supersaturated Au–Ni nanoparticles *via* dewetting of an Au/Ni bilayer, Mater. Lett. 102-103 (2013) 22–25.

[46] A. Herz, D. Wang, P. Schaaf, Dewetting of Au/Ni bilayer films on prepatterned substrates and the formation of arrays of supersaturated Au-Ni nanoparticles, J. Vac. Sci. Technol. B Nanotechnol. Microelectron. Mater. Process. Meas. Phenom. 32 (2) (2014).

[47] A. Herz, et al., Solid-state dewetting of Au/Ni bilayers: the effect of alloying on morphology evolution, J. Appl. Phys. 116 (4) (2014).

[48] X. Cen, A.M. Thron, K. van Benthem, *In-situ* study of the dewetting behavior of Au/Ni bilayer films supported by a SiO2/Si substrate, Acta Mater. 140 (2017) 149–156.

[49] X. Cen, et al., Cross-sectional characterization of the dewetting of a Au/Ni bilayer film, Ultramicroscopy 178 (2017) 131–139.

[50] J.E. Bruno, et al., Supported Ni–Au colloid precursors for active, selective, and stable alkyne partial hydrogenation catalysts, ACS Catal. 10 (4) (2020) 2565–2580.

[51] B. Roldan Cuenya, Metal nanoparticle catalysts beginning to shape-up, Acc. Chem. Res. 46 (8) (2012) 1682–1691.

[52] H. Lee, Utilization of shape-controlled nanoparticles as catalysts with enhanced activity and selectivity, RSC Adv. 4 (77) (2014) 41017–41027.

[53] S.A. Nikolaev, V.V. Smirnov, Synergistic and size effects in selective hydrogenation of alkynes on gold nanocomposites, Catal. Today 147 (2009) S336–S341.

[54] S.A. Nikolaev, et al., Synergism of the catalytic effect of nanosized gold-nickel catalysts in the reaction of selective acetylene hydrogenation to ethylene, Kinet. Catal. 51 (3) (2010) 375–379.

[55] M. Chai, et al., SiO2 -supported Au-Ni bimetallic catalyst for the selective hydrogenation of acetylene, Chin. J. Catal. 38 (8) (2017) 1338–1346.

[56] T. Ward, et al., Effects of Pd on Catalysis by Au: CO adsorption, CO oxidation, and cyclohexene hydrogenation by supported Au and Pd-Au catalysts, ACS Catal. 3 (11) (2013) 2644–2653.

[57] G. Giannakakis, et al., NiAu single atom alloys for the non-oxidative dehydrogenation of ethanol to acetaldehyde and hydrogen, Top. Catal. 61 (5–6) (2018) 475–486.

[58] G. Kyriakou, et al., Comprehensive experimental and theoretical study of the CO + NO reaction catalyzed by Au/Ni nanoparticles, ACS Catal. 9 (6) (2019) 4919–4929.

[59] S. Zhou, et al., Low-temperature solution-phase synthesis of NiAu alloy nanoparticles via butyllithium reduction: influences of synthesis details and application as the precursor to active Au-NiO/SiO2 catalysts through proper pretreatment, J. Phys. Chem. C 113 (14) (2009) 5758–5765.

[60] D. Amram, E. Rabkin, Core(Fe)-shell(Au) nanoparticles obtained from thin Fe/Au bilayers employing surface segregation, ACS Nano 8 (10) (2014) 10687–10693.

[61] S. Lee, et al., FIB-induced dislocations in Al submicron pillars: annihilation by thermal annealing and effects on deformation behavior, Acta Mater. 110 (2016) 283–294.

[62] D. Mordehai, et al., Size effect in compression of single-crystal gold microparticles, Acta Mater. 59 (13) (2011) 5202–5215.

[63] W.M. Mook, et al., Compression of freestanding gold nanostructures: from stochastic yield to predictable flow, Nanotechnology 21 (5) (2010).

[64] Z.J. Wang, et al., Pristine-to-pristine regime of plastic deformation in submicron-sized single crystal gold particles, Acta Mater. 60 (3) (2012) 1368–1377.

[65] A. Sharma, et al., Pseudoelasticity of metal nanoparticles is caused by their ultrahigh strength, Adv. Funct. Mater. 30 (18) (2019).

[66] A. Sharma, et al., Nickel nanoparticles set a new record of strength, Nat. Commun. 9 (1) (2018).

[67] A. Herz, et al., Solid-state dewetting of Au-Ni bi-layer films mediated through individual layer thickness and stacking sequence, Appl. Surf. Sci. 444 (2018) 505–510.

[68] Herz, A., On the solid-state dewetting of Au-Ni and Au-W bilayer polycrystalline thin films and the formation of alloy micro- and nanoparticles. 2016. https://www.db-thueringen.de/receive/dbt_mods_00030828.

[69] J.C. Zhao, M.R. Notis, Ordering transformation and spinodal decomposition in Au-Ni alloys, Metall. Mater. Trans. A 30 (3) (1999) 707–716.

[70] P. Herre, et al., Deformation behavior of nanocrystalline titania particles accessed by complementary *in situ* electron microscopy techniques, J. Am. Ceram. Soc. 100 (12) (2017) 5709–5722.

[71] J. Schwenger, et al., Pressure induced local phase transformation in nanocrystalline tetragonal zirconia microparticles, Scr. Mater. 163 (2019) 86–90.

[72] S. Romeis, et al., A novel apparatus for *in situ* compression of submicron structures and particles in a high resolution SEM, Rev. Sci. Instrum. 83 (9) (2012).

[73] R. Kaishew, Equilibrium shape and nucleation work of crystals on substrates, Commun. Bulg. Acad. Sci. 1 (1950) 100–139.

[74] W.L. Winterbottom, Equilibrium shape of a small particle in contact with a foreign substrate, Acta Metall. 15 (2) (1967) 303–310.

[75] R.V. Zucker, et al., New software tools for the calculation and display of isolated and attached interfacial-energy minimizing particle shapes, J. Mater. Sci. 47 (24) (2012) 8290–8302.

[76] J. Brillo, I. Egry, Surface tension of nickel, copper, iron and their binary alloys, J. Mater. Sci. 40 (9–10) (2005) 2213–2216.

[77] G. Levi, W.D. Kaplan, Aluminium-alumina interface morphology and thermodynamics from dewetting experiments, Acta Mater. 51 (10) (2003) 2793–2802.

[78] J. Frenkel, Zur theorie der elastizittsgrenze und der festigkeit kristallinischer krper, Z. Phys. 37 (7–8) (1926) 572–609.

[79] J.S. Hong, et al., Equilibrium shape of nickel crystal, Philos. Mag. 89 (32) (2009) 2989–2999.

[80] P. Müller, R. Kern, Equilibrium nano-shape changes induced by epitaxial stress (generalised Wulf–Kaishew theorem), Surf. Sci. 457 (1) (2000) 229–253.

[81] J.C. Heyraud, J.J. Métois, Growth shapes of metallic crystals and roughening transition, J. Cryst. Growth 82 (3) (1987) 269–273.

[82] D. Chatain, Anisotropy of wetting, Annu. Rev. Mater. Res. 38 (1) (2008) 45–70.

[83] H. Nahor, Y. Kauffmann, W.D. Kaplan, The Cr-doped Ni-YSZ(111) interface: segregation, oxidation and the Ni equilibrium crystal shape, Acta Mater. 166 (2019) 28–36.

[84] D. Chatain, P. Wynblatt, G.S. Rohrer, Equilibrium crystal shape of bi-saturated Cu crystals at 1223 K, Acta Mater. 53 (15) (2005) 4057–4064.

[85] W.C. Cheng, P. Wynblatt, Equilibrium form of Pb bi Ni alloy crystals, J. Cryst. Growth 173 (3–4) (1997) 513–527.

[86] J.E. Reynolds, B.L. Averbach, M. Cohen, Self-diffusion and interdiffusion in gold-nickel alloys, Acta Metall. 5 (1) (1957) 29–40.

[87] L. Vegard, Die konstitution der mischkristalle und die raumfüllung der atome, Z. Phys. 5 (1) (1921) 17–26.

[88] J.R. Clinton, E.H. Tyler, H.L. Luo, Electrical and magnetic properties of Au-Ni alloys, J. Phys. F Met. Phys. 4 (8) (1974) 1162–1169.

[89] J. Eymery, F. Lançon, L. Billard, Au-Ni solid solutions studied by numerical relaxation, J. Phys. I 3 (3) (1993) 787–802 France.

[90] G. Renaud, et al., Topological short-range disorder in Au$_{1-x}$Ni$_x$ solid solutions: an extended x-ray-absorption fine-structure spectroscopy and computer-simulation study, Phys. Rev. B 38 (9) (1988) 5944–5964.

[91] F. Niekiel, et al., Texture evolution and microstructural changes during solid-state dewetting: a correlative study by complementary *in situ* TEM techniques, Acta Mater. 115 (2016) 230–241.

[92] M.J. Kelley, P.W. Gilmour, D.G. Swartzfager, Strain effects in surface segregation-the Au/Ni system, J. Vac. Sci. Technol. 17 (2) (1980) 634–637.

[93] W.C. Johnson, et al., Orientation dependence of surface segregation in a dilute Ni-Au alloy, J. Vac. Sci. Technol. 15 (2) (1978) 467–469.

[94] D.A. Steigerwald, S.J. Miller, P. Wynblatt, Anisotropy of surface composition in a Ni-Au alloy, Surf. Sci. 155 (1) (1985) 79–100.

[95] H. Nahor, et al., Discerning interface atomistic structure by phase contrast in STEM: the equilibrated Ni-YSZ interface, Acta Mater. 154 (2018) 71–78.

[96] S. Choudhury, et al., Non-uniform solute segregation at semi-coherent metal/oxide interfaces, Sci. Rep. 5 (1) (2015).

[97] S.J. Pennycook, P.D. Nellist, Z-Contrast Scanning Transmission Electron Microscopy, in: D.G. Rickerby, G. Valdrè, U. Valdrè (Eds.), Impact of Electron and Scanning Probe Microscopy on Materials Research, Springer Netherlands, Dordrecht, 1999, pp. 161–207.

[98] Z. Yu, D.A. Muller, J. Silcox, Study of strain fields at a-Si/c-Si interface, J. Appl. Phys. 95 (7) (2004) 3362–3371.

[99] M.Y. Gutkin, A.E. Romanov, On the stand-off positions of misfit dislocations, Phys. Status Solidi A 144 (1) (1994) 39–57.

[100] H. Li, et al., Strong metal–metal interaction and bonding nature in metal/oxide interfaces with large mismatches, Acta Mater. 179 (2019) 237–246.

[101] G. Pilania, et al., Revisiting the Al/Al$_2$O$_3$ interface: coherent interfaces and misfit accommodation, Sci. Rep. 4 (1) (2014).

[102] P. Lazar, et al., Interface structure of epitaxial (111) VN films on (111) MgO substrates, Thin Solid Films 517 (3) (2008) 1177–1181.

[103] H.B. Groen, et al., High-resolution transmission electron microscopy imaging of misfit-dislocation networks at Cu-MgO and Cu-MnO interfaces, Philos. Mag. A 79 (9) (1999) 2083–2101.

[104] P.H. Dederichs, The theory of diffuse X-ray scattering and its application to the study of point defects and their clusters, J. Phys. F Met. Phys. 3 (2) (1973) 471–496.

[105] C. Bergmann, et al., Strain relief via silicon self-interstitial emission in highly boron-doped silicon: a diffuse X-ray scattering study of oxygen precipitation, J. Appl. Phys. 118 (1) (2015) 015707.

[106] S.I. Olikhovskii, et al., Generalized statistical dynamical theory of X-ray diffraction by imperfect multilayer crystal structures with defects, Phys. Rev. B 99 (23) (2019) 235304.

[107] M.D. Uchic, P.A. Shade, D.M. Dimiduk, Micro-compression testing of fcc metals: a selected overview of experiments and simulations, JOM 61 (3) (2009) 36–41.

[108] R. Maaß, P.M. Derlet, Micro-plasticity and recent insights from intermittent and small-scale plasticity, Acta Mater. 143 (2018) 338–363.

[109] A.Z.M.A. Islam, R.J. Klassen, Kinetics of length-scale dependent plastic deformation of gold microspheres, J. Mater. Res. 32 (18) (2017) 3507–3515.